In vivo optical characterization of human prostate tissue using near-infrared time-resolved spectroscopy

Tomas Svensson
Stefan Andersson-Engels
Lund University
Department of Physics
SE-221 00 Lund
Sweden

Margrét Einarsdóttír
Katarina Svanberg
Lund University Hospital
Department of Oncology
SE-221 00 Lund
Sweden

Abstract. The development of photodynamic therapy into a modality for treatment of prostate cancer calls for reliable optical dosimetry. We employ, for the first time, interstitial time-resolved spectroscopy to determine *in vivo* optical properties of human prostate tissue. Nine patients are included in the study, and measurements are conducted prior to primary brachytherapy treatment of prostate cancer. Intrasubject variability is examined by measuring across three tissue volumes within each prostate. The time-resolved instrumentation proves its usefulness by producing good signal levels in all measurements. We are able to present consistent values on reduced scattering coefficients (μ_s'), absorption coefficients (μ_a), and effective attenuation (μ_{eff}) at the wavelengths 660, 786, and 916 nm. At 660 nm, μ_s' is found to be 9 ± 2 cm^{-1}, and μ_a is 0.5 ± 0.1 cm^{-1}. Derived values of μ_{eff} are in the range of 3 to 4 cm^{-1} at 660 nm, a result in good agreement with previously published steady state data. Total hemoglobin concentration (THC) and oxygen saturation are spectroscopically determined using derived absorption coefficients. Derived THC values are fairly variable (215 ± 65 μM), while derived values of oxygen saturation are gathered around 75% (76 ± 4%). Intrasubject variations in derived parameters correlate (qualitatively) with the heterogeneity exhibited in acquired ultrasound images. [DOI: 10.1117/1.2435175]

Keywords: human prostate; hemoglobin; photon migration; time-resolved spectroscopy; optical properties; *in vivo*.

Paper 06239R received Sep. 5, 2006; revised manuscript received Nov. 7, 2006; accepted for publication Nov. 8, 2006; published online Jan. 25, 2007.

1 Introduction

Interest in optical characteristics of the human prostate is mainly related to recent efforts in developing photodynamic therapy (PDT) into a modality for treatment of localized prostate cancer. Initial preclinical work on PDT of prostate carcinoma appeared during the 1980s (Refs. 1 and 2) and (first) clinical work was published[3] as early as 1990. For the development and optimization of the technique, several studies have since been performed on canine[4–6] and rat[1,7] models. Clinical results from various research groups are now available.[8–13] Altogether, these results have shown a great potential of PDT in the management of prostate cancer.[14,15]

PDT, in general, relies on a process where light excites (i.e., activates) a photosensitizer, which induces cytotoxic oxygen species. Thus, PDT relies on the presence of light, a photosensitizer, and oxygen. The corresponding dosimetry is therefore a complex matter, involving measurement and/or prediction of sensitizer and oxygen concentrations as well as light fluence (light dose). Since full treatment of diseased regions is crucial, these issues must be carefully addressed. Accordingly, PDT dosimetry has been the main focus of numerous papers (see, e.g., Star[16]), of which a few are closely related to the particular case of PDT of prostate cancer.[17–21] One fundamental aspect in this context is the tissue optical properties, e.g., absorption and scattering coefficients. Not only do they together determine the light dose distribution, but *in vivo* access to absorption coefficients can be used to estimate, for example, sensitizer concentrations, hemoglobin concentration, and tissue oxygenation. In addition, due to dynamic changes during PDT treatment, it is sometimes argued that on-line monitoring is required to achieve optimal treatment.[22,23]

For the case of prostate tissue, several papers have addressed the issue of optical properties, e.g., the effective attenuation coefficient μ_{eff} and in some cases also absorption and reduced scattering coefficients μ_a and μ_s', respectively.[4,18,24–31] Most of them rely on interstitial fiber optic steady state fluence rate measurements at multiple source-detector separations. By measuring relative fluence rate in a range of source-detector separations larger than a few millimeters (i.e., the diffuse regime), the diffusion approximation of light transport can be employed to determine μ_{eff}. Since μ_{eff} depends on both μ_a and μ_s', additional data is required to reach information on absorption and scattering separately.

Address all correspondence to Tomas Svensson, Department of Physics, Lund University, Box 118, SE-221 00 Lund, Sweden; Phone: +46-46-2223120; Fax: +46-46-2224250; E-mail: tomas.svensson@fysik.lth.se

1083-3668/2007/12(1)/014022/10/$25.00 © 2007 SPIE

One option is to determine $\mu_t' = \mu_a + \mu_s'$ by measuring relative radiance at multiple, but short, source-detector separations.[32] A second option, avoiding the need of short source-detector separations, is to measure absolute (instead of relative) fluence rate in the diffuse regime.[33] Data evaluation, by means of curve fitting, then yields μ_{eff} and μ_s'. Hence, both options enable estimation of absorption and scattering coefficients.

Previously published values on optical properties of the human prostate, together with the results obtained in this study, are given in Sec. 3. The first published work presents *ex vivo* steady state measurements of μ_{eff} and $\mu_t' = \mu_a + \mu_s'$, at 633 nm, in three whole, nonmalignant human prostates.[24] Another *post mortem* study estimates prostate optical properties (μ_a, scattering coefficient μ_s, scattering anisotropy g, and μ_s') at 1064 nm, by measuring through thin prostate slices.[25] *In vivo* effective attenuation in prostates diagnosed with benign prostatic hyperplasia (BPH) or prostatic carcinoma (PC) has been estimated at 630, 633, and 665 nm, by employing steady state fluence rate measurements.[26,28,29] Other studies rely on absolute fluence rate measurements to determine both absorption and scattering coefficients. By measuring fluence rates along a linear channel (5 mm away from the source fiber), one such study presents optical properties at 732 nm, before and after motexafin-lutetium-mediated PDT of locally recurrent prostate cancer.[34] In a similar study, optical fibers are kept fixed (five source fibers and three detector fibers), and absolute fluence rate data is collected for 15 source-detector separations (at 762 nm). Measurements were in that case performed in connection with TOOKAD-mediated PDT of recurrent prostate cancer.[30] Regarding hemoglobin monitoring in human subjects, only very limited data have been published.[30,31]

This study employs interstitial time-resolved spectroscopy to characterize human prostate tissue *in vivo*. Conceptually, this approach is very different from those chosen in previously published work related to prostate tissue. By analyzing the temporal broadening of picosecond laser pulses due to propagation through tissue, this technique provides reliable estimations of absorption and reduced scattering coefficients. The use of multiple wavelengths enables spectroscopic determination of total hemoglobin concentration (THC) and oxygen saturation (S_tO_2). The technique has previously been used in various areas of biomedical optics.[35–39]

The aim of the paper is to provide information on parameters of dosimetric importance, as well as to introduce time-resolved spectroscopy as a tool in PDT research. In particular, the aim is to achieve separate information on μ_a and μ_s', as well as quantitative information on hemoglobin parameters. We also wish to give a proper indication on intra- and inter-subject variation, for the case of untreated prostate cancer. These parameters are important for PDT dosimetry calculations, and are not extensively explored in previous studies.

Nine patients diagnosed with prostate cancer were included in the study, and all measurements were performed before primary treatment. By inserting three optical fibers, three tissue volumes were probed, yielding information on prostate tissue heterogeneity.

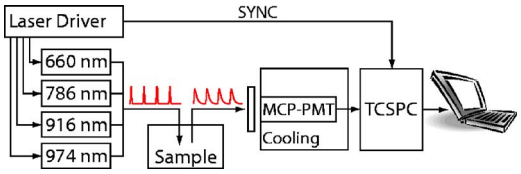

Fig. 1 Schematic of the instrumentation in interstitial mode.

2 Material and Methods

2.1 *Instrumentation*

Time-resolved data were acquired using a compact ($50 \times 50 \times 30$ cm) and portable time-domain photon migration instrument primarily intended for spectroscopy of biological tissues in clinical environments.[39,40] A schematic illustration is given in Fig. 1.

The system is based on diode laser technology and time-correlated single-photon-counting (TCSPC). A laser driver (SEPIA PDL 808, PicoQuant, Germany) controls four pulsed diode lasers (LDH, PicoQuant at 660, 786, 916, and 974 nm). Wavelengths are chosen to enable monitoring of important tissue constituents (hemoglobin, water, and lipids) and properties (tissue oxygenation). Lasers are typically operated at 1 to 2 mW, generating pulses about 70 ps wide (FWHM). Four wavelength pulse trains are generated at a repetition frequency of 40 MHz. This is accomplished by separating the individual pulses in time (~6 ns), using electric cables of different lengths.

The light emitted from each diode laser is individually coupled into a separate 200-μm graded-index (GRIN) fiber (G 200/280 N, ART Photonics, Germany). A four-to-one coupler is used to couple all light into a single 600-μm GRIN fiber (G 600/840 P, ART Photonics), which serves as the light source. A second fiber collects light and delivers it to the detector. Each of these two fibers is approximately 2 m long. To fit into 1-mm inner diameter brachytherapy needles, a thin polyimide layer acts as the only fiber coating at the fiber endings. Remaining parts are protected in polyolefin tubing.

Proper photon levels are achieved by sending collected light through an adjustable gradient neutral density (ND) filter. Remaining photons are sent to a cooled microchannel plate photomultiplier tube (MCP-PMT; R3809-59, Hamamatsu Photonics, Japan). A TCSPC computer card (SPC-300, Becker&Hickl, Germany) is used to obtain time-dispersion histograms with channel widths of approximately 25 ps.

Broadening in the fibers and the detector yields an instrument response function (IRF) that is about 100 ps wide. The IRF is measured by inserting source and detector fibers into a chamber so that the end facets are separated by 150 mm and face each other. The chamber is made of black delrin, and contains a pinhole that is inserted between the two fibers to block reflected stray light.

2.2 *Modeling*

Experimental data are modeled using the diffusion approximation of transport theory. More specifically, data are fitted to the analytical solution of the time-dependent diffusion equation for the case of a homogenous and infinite medium.[41]

Accordingly, the fluence rate Φ due to a infinitely short light pulse from an isotropic point source can be written as

$$\Phi(r,t) = c' E_0 (4\pi c' D t)^{-3/2} \exp\left(-\frac{r^2}{4c'Dt} - \mu_a c' t\right), \quad (1)$$

where E_0 is the pulse energy, r is the distance from the point source, c' is the speed of light within the material, and D is the diffusion coefficient. The refractive index is assumed to be $n=1.4$. To comply with recent work concerning the diffusion coefficient, it is defined as in Eq. (2), rather than in the traditional (absorption-dependent) way[42,43]:

$$D = \frac{1}{3\mu_s'}. \quad (2)$$

The form of Eq. (1) enables deduction of both μ_s' and μ_a from experimental data without requiring absolute measurements of light fluence. This is achieved by considering temporal shapes only. That is, experimental data are fitted using an expression similar to that given in Eq. (1), but in which amplitude information is contained in a free parameter k. This expression is given as

$$y(\mu_a, \mu_s', k, t) = k\, t^{-3/2} \exp\left(-\frac{3\mu_s' r^2}{4c't} - \mu_a c' t\right). \quad (3)$$

The best fit is reached iteratively using a Levenberg-Marquardt algorithm, where μ_s', μ_a, and k are varied to minimize a χ^2 error norm.[44] Final values of μ_s' and μ_a are then estimations of the reduced scattering coefficient and absorption coefficient, respectively. Note that the IRF, being about 100 ps wide, cannot be regarded as infinitely short in comparison to the tissue response. Therefore, each iteration in the curve-fitting procedure involves a convolution of analytical data and IRF. It should also be noted that fitting is performed using the part of experimental data between times given by the 50% of maximum on the rising edge, and 20% on the falling edge (see Fig. 5 in Sec. 3).

The previous studies of human prostate optical properties mentioned in the introduction used the same theoretical framework. However, by employing steady state techniques, they rely on a stationary solution rather that the time-dependent solution given in Eq. (1). The stationary solution of the diffusion equation for an infinite homogenous medium is given as

$$\Phi(r) = \frac{3\mu_s' P_0}{4\pi r} \exp(-\mu_{\text{eff}}\, r). \quad (4)$$

Here, P_0 is the power of the point source, r is the distance from the source, and μ_{eff} the effective attenuation. The effective attenuation is defined as

$$\mu_{\text{eff}} = (\mu_a/D)^{1/2} = (3\mu_a\mu_s')^{1/2} \quad (5)$$

From the form of Eq. (4), we see that μ_{eff} can be deduced from relative fluence measurements at multiple source detector separations. Only if absolute fluence rate is measured, it can be used to get information on reduced scattering and absorption separately. Absolute measurement of fluence rate in living tissue is of course a difficult matter (especially in interstitial settings). Note also that μ_{eff} is a primary parameter when using the steady state technique. Time-resolved experiments provide estimations of μ_a and μ_s' which in a second step can be used to calculate μ_{eff}.

Table 1 Extinction and absorption coefficients of tissue chromophores.

	Unit	660 nm	786 nm
Pure water	cm^{-1}	0.0036	0.0222
Pure lipid	cm^{-1}	0.0042	0.0036
Hb	$cm^{-1}/\mu M$	0.0074	0.0022
HbO_2	$cm^{-1}/\mu M$	0.00074	0.0017

2.3 *Hemoglobin Spectroscopy*

The spectroscopic evaluation employed in this study assumes that the absorption exhibited by prostate tissue originates from oxy- and deoxyhemoglobin (Hb and HbO_2, respectively), water, and lipids. Since high absorption prevented the use of 974-nm data (see Sec. 3), water and lipid concentrations could not be estimated. Instead, absorption coefficients at 660 and 786 nm were used to extract oxy- and deoxyhemoglobin concentrations ($[HbO_2]$ and [Hb], respectively). In this procedure, the prostate was assumed to contain 70% water and 10% lipids (note that due to relatively low absorption of water and lipids at 660 and 786 nm, the choice of these values is of very little importance). The extinction coefficients of these chromophores were taken from literature[45–47] and are presented in Table 1.

In a second step, total hemoglobin concentration and oxygen saturation are calculated from $[HbO_2]$ and [Hb].

2.4 *Clinical Procedure*

Clinical data were collected at the Lund University Hospital adhering to a protocol approved by the regional ethics committee. All nine patients involved in the study were undergoing primary treatment of prostate cancer. Measurements were performed in connection with brachytherapy (low-dose seed implantation). This fact limits our study to patients suitable for this treatment, that is, patients fulfilling the following requirements: (1) Gleason index <6, (2) prostate specific antigen (PSA) <10, (3) no tumor obstruction of urethra, and (4) prostate volume of the order of 20 to 40 cm^3. Such patients are often referred to as low-risk patients.

This type of brachytherapy of prostate cancer involves permanent implantation of radioactive seeds (internal radiotherapy). The procedure takes place in an operating theater, while patients are under general anesthesia. At the Lund University Hospital, the first step in this procedure is to image the prostate gland using transrectal ultrasound. When the physician has marked important boundaries in these images (prostate, urethra, and rectum), a radiotherapist performs dosimetric calculations. Dosimetric calculations open a time window of about 20 min in which the time-resolved measurements were performed without interfering with the routine proce-

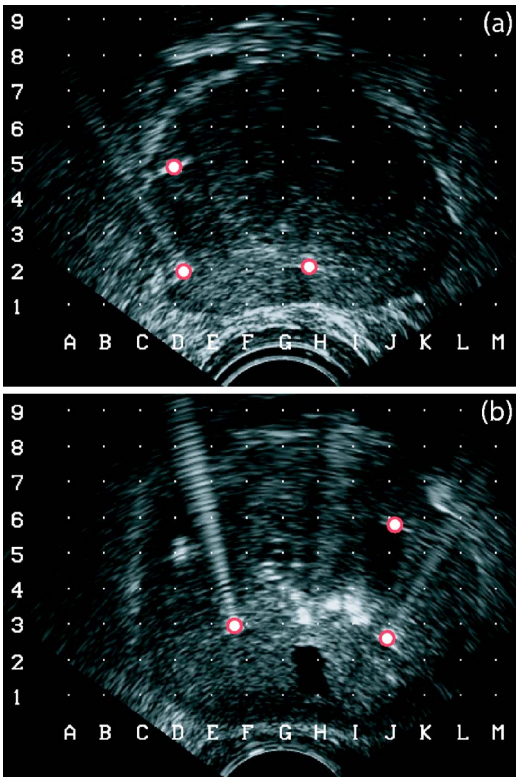

Fig. 2 Two ultrasound images showing three needles inserted into the prostate. For clarity, the needles are marked by circles. Shadows behind the needles are due to their high reflectivity. The fairly homogenous image (a) originates from patient 5, while the heterogenous structure in (b) was exhibited by patient 6.

dures. Three standard brachytherapy needles were then inserted, all to the same depth (using transrectal ultrasound guidance). A standard transperineal brachytherapy needle matrix handles lateral positioning (5×5-mm grid spacing). Three sterilized optical fibers were inserted through the three needles so that they were located edge to edge with the needle tips (this positioning is achieved by premarking the fibers). Fiber separations are inferred from ultrasound images (B-K Medical Hawk 2102 EXL with transducer 8658-T operating at 6.5 to 7.5 MHz). Figure 2 shows two authentic ultrasound images.

By using three needles, it is possible to probe three fairly nonoverlapping prostate tissue volumes. Fiber separations were in the range of 10 to 30 mm. The three fiber separations used within each patient were chosen to differ, and typically set in a triangular pattern to approximately 15, 20, and 25 mm. The longest fiber separation corresponds to a more central volume of the prostate, bordering the urethra. Typical fiber positioning is schematically illustrated in Fig. 3. In addition, this figure also indicates sampling volumes by displaying[48] PHDs.

Since the instrumentation used in this study supports only one source and one detector fiber at a time, three sequential measurements must be performed. The total data acquisition time was approximately 3 min per patient (1 min per tissue volume). To detect unexpected changes during data acquisition, measurements were performed in 1 s increments. After

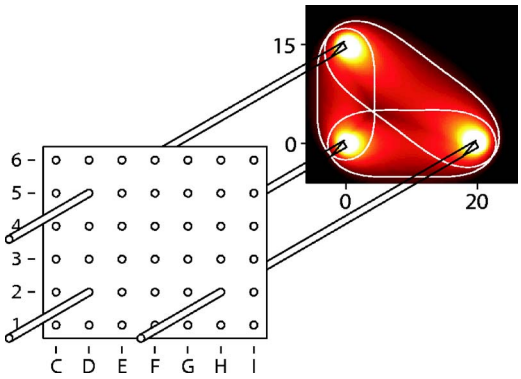

Fig. 3 Schematic drawing of fiber positioning [compare with Fig. 2(a)]. The needle template has 5-mm grid spacing. Three optical fibers are inserted to the same depth. Fiber separations are 15, 20, and 25 mm. The three tissue volumes being probed are indicated using calculations of photon-hitting densities (PHDs) at the plane of fiber tips ($\mu_s'=8.7$ and $\mu_a=0.49$ cm^{-1}). Isocurves indicate where the PHD is 50% of the value exhibited halfway between source- and detector fibers.

completion of the tissue measurements, the IRF is measured using the same set of fibers. To ensure system stability (e.g., avoid drifts due to temperature changes), this step is conducted while the system is in the operating theater.

3 Results

Analysis of collected data reveals that time-resolved spectroscopy can provide consistent optical and physiological characteristics of human prostate tissue. Data were collected at four wavelengths: 660, 786, 916, and 974 nm. For each patient and wavelength, raw data consist of three dispersion curves (tissue response) corresponding to the three utilized fiber separations (in total, 27 time-resolved data sets from nine patients). Since the fiber separations within a patient are chosen to be different, e.g., 15, 20, and 25 mm, the obtained curves are significantly different. For the range of fiber separations used in this study, most detected light travels a time less than 1.5 ns through tissue (corresponding to maximum path lengths of about 30 cm). An example of raw data, for the case of 660 nm, is given in Fig. 4.

By means of curve fitting, optical properties were extracted for 660, 786, and 916 nm from all 27 time-resolved data sets. Unfortunately, high absorption at 974 nm prevented analysis of data acquired at that wavelength. A typical fitting example, for the case of 786 nm, is shown in Fig. 5.

A summary of the results of this study is given in Table 2, in which previously published data are presented for comparison. A detailed report on measured optical (at 660 and 786 nm) and physiological characteristics are given in Table 3. In the following, graphical representation of data from Table 3 is used to illustrate and support further analysis.

No pronounced correlation between estimated values of μ_a and μ_s' was seen for any wavelength, implying that results do not suffer from μ_s' to μ_a crosstalk. This is shown in Fig. 6, where results from 660 nm are presented. A general comment is, however, helpful in interpreting the pattern shown. Three measurements (21.5 and 26.4 mm from patient 6, and 25.0 mm from patient 8) resulted in very low values of both

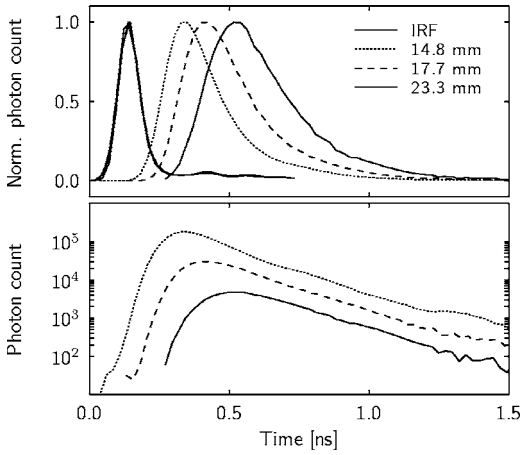

Fig. 4 Acquired time-resolved data at 660 nm for patient 5 (after background subtraction). Data are shown in both linear (upper axes, normalized) and logarithmic scale (lower axes). Corresponding 660-nm IRFs are also shown. Input laser pulses are broadened from 90 ps (IRF) to 222 (14.8), 264 (17.7), and 291 ps (23.3 mm).

absorption and reduced scattering (leading to a THC less than 100 μM). In these cases, note that an extremely low degree of bleeding was noted during the measurements (almost no blood stains on the used fibers, while the average fiber was heavily stained after a measurement). Thus, it is likely that these measurement outcomes correspond to a particular tissue composition, rather than a systematic error such as μ_s' to μ_a crosstalk.

The influence of fiber separation on derived optical properties is illustrated in Fig. 7. Although derived optical properties show no strict dependence on the fiber separation, there might be a tendency toward measuring lower μ_a and μ_s' for large fiber separations. Such a tendency may be related to the fact that the longest fiber separation (for each patient) corresponds to a central prostate volume, while the two shorter correspond to outer volumes. For comparison, note that studies on intralipid phantoms having prostate-like optical properties were performed. In these, the selection of fiber separation had no systematic influence on derived optical properties.

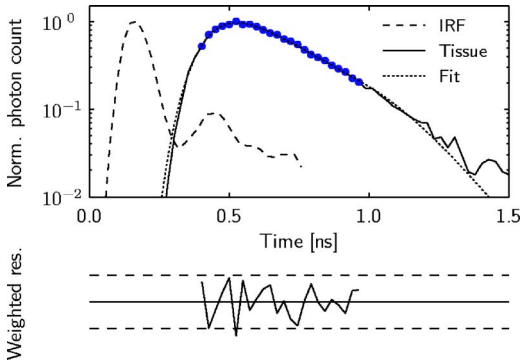

Fig. 5 Fitting of 786-nm time-resolved data from patient 4 (26.5-mm fiber separation). Dispersion data used in fitting are marked by solid dots. Weighted residuals are shown below, together with the zero level (solid line) and the [−1.96, 1.96] prediction interval of standardized normal distributions (dashed lines).

As we can see in Fig. 8, derived hemoglobin concentrations show a behavior similar to that of μ_a, while oxygen saturation showed no correlation to utilized fiber separation.

Turning to inter- and intrapatient variations, an important general observation is that patients 2 to 5 exhibited homogenous ultrasound images, while obvious inhomogeneities due to calcifications are found in images from patients 1 and 6 to 9. As we can see in Figs. 9–11, this fact correlates to measured intrasubject variations. A second general observation is that all derived parameters, except oxygen saturation, can be subject to a fairly large spread, even within individual patients. Figure 9 presents inter- and intrapatient variations of 660-nm optical properties.

Effective attenuation, being an important parameter in PDT dosimetry, was calculated from extracted μ_a and μ_s' and is presented in Fig. 10.

Hemoglobin concentrations and oxygen saturation were spectroscopically determined using absorption coefficients as measured at 660 and 786 nm. As we can see in Fig. 11, THC exhibit substantial inter- and intrasubject variations. Oxygen saturation, on the other hand, displays only minor variations.

One alternative to deriving hemoglobin concentrations from 660- and 786-nm data only, would be to include 916-nm data (still assuming that the prostate contains 70% water and 10% lipids). If this procedure is followed, resulting THC values deviate by +1.5±8.7%, and S_tO_2 by +1.1±4.1% from the values calculated from 660- and 786-nm data only. In terms of overall impact, derived THC changes from 215±65 to 215±56 μM (the rounded average is coincidentally conserved), and S_tO_2 from 76±4 to 77±4%. These fairly small changes can also be understood by analyzing the difference between measured 916-nm μ_a, and the predicted 916-nm μ_a, as calculated from derived hemoglobin levels (estimated from 660- and 786-nm data) in combination with the assumption of 70% water and 10% lipids. Such analysis show that measured 916-nm μ_a deviates by 2±11% from predicted values.

A synthetic absorption spectra can be constructed using derived hemoglobin concentrations and assumed concentrations of water and lipids. Figure 12 presents the average composite absorption spectra of the prostate, as derived in this study.

4 Discussion

Reliable optical dosimetry is an important issue in the development of PDT into a modality for treatment of prostate can-

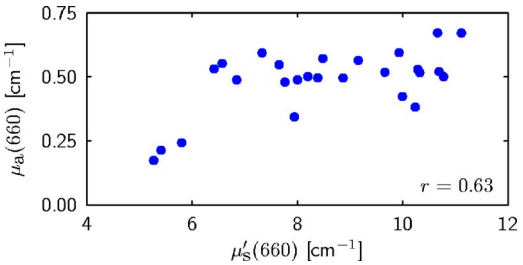

Fig. 6 Scatterplot showing correlation between derived μ_s' and μ_a at 660 nm. The three points in the lower left correspond to the three measurement cases exhibiting a low degree of bleeding and low THC (r=0.31 if disregarded).

Table 2 Optical properties (given in inverse centimeters) of human prostate tissue as reported in various published studies; the number of involved patients is also given (*N*); note differences regarding wavelength.

Study	Description	λ (nm)	*N*	μ_a	μ_s'	μ_{eff}
Pantelides et al.[24] (1990)	*ex vivo* steady state data, normal whole prostates	633	3	0.7±0.2	8.6±0.5	4.3±0.5
Whitehurst et al.[26] (1994)	*in vivo* steady state data, untreated BPH and PC	633	11			3.6±0.2
Lee et al.[28] (1995)	*in vivo* steady state data, untreated BPH and PC	633	11			3.9±0.5
Lee et al.[28] (1995)	*in vivo* steady state data, untreated BPH and PC	665	11			3.2±0.5
Lee et al.[29] (1999)	*in vivo* steady state data, untreated PC	630	7			3.5±0.7
This study	*in vivo* time-resolved data, untreated PC	660	9	0.5±0.1	8.7±1.9	3.6±0.8
Weersink et al.[30] (2005)	*in vivo* steady state data, recurrent PC	762	22	0.4±0.2	3.4±1.6	2.0±0.6
Zhu et al.[34] (2005)	*in vivo* steady state data, recurrent PC	732	13	0.4±0.2	11.8±8.2	3.3±0.5
This study	*in vivo* time-resolved data, untreated PC	786	9	0.4±0.1	7.1±1.6	2.9±0.7
This study	*in vivo* time-resolved data, untreated PC	916	9	0.6±0.1	7.7±1.8	3.8±0.8
Essenpreis et al.[25] (1992)	*ex vivo* integrating sphere data, normal prostates	1064		1.5±0.2	6.4	

cer. Whether reliable dosimetry means on-line monitoring of certain parameters, individual pretreatment planning, or general knowledge on intra- and intersubject variations remains an open question. By employing time-resolved spectroscopy, this study was able to generate estimations of optical and physiological characteristics (μ_a, μ_s', μ_{eff}, total hemoglobin concentration, and oxygen saturation) for all involved patients, and thus providing a reliable indication on intra- and intersubject variations for the case of untreated prostate cancer. In fact, as we can see in Table 3, all measurements resulted in quality data. In addition, by requiring only two fixed fibers for a single measurement, the time-resolved technique is accompanied with fairly simple clinical procedures.

Calculations of PHDs suggest that sampling volumes are kept within the prostate. Results are consistent and imply that the prostates of the patient group under consideration exhibit moderate intra- and intersubject variations. However, the fol-

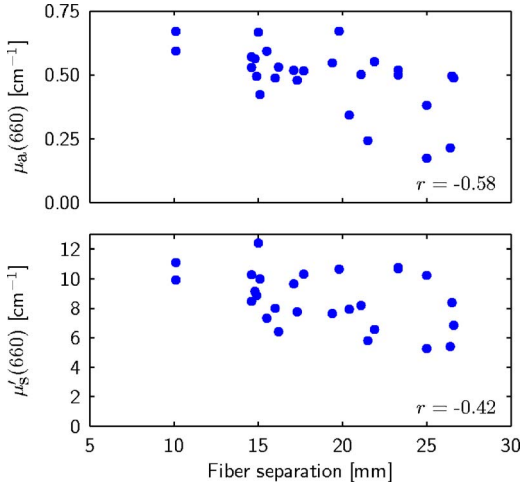

Fig. 7 Scatterplot showing the correlation between utilized fiber separation and derived optical properties at 660 nm. Correlation coefficients *r* are added for reference. The three points with $\mu_a < 0.25$ correspond to the three measurement cases exhibiting a low degree of bleeding and low THC.

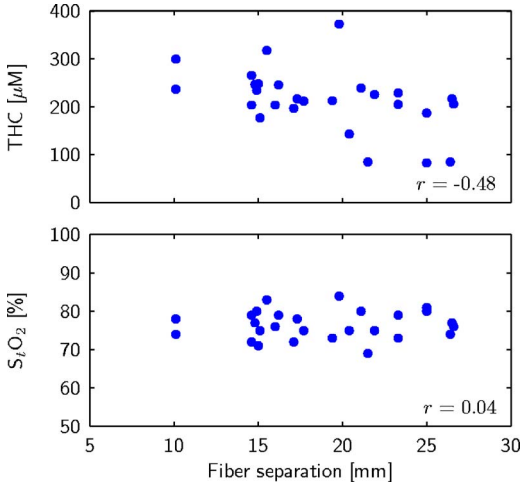

Fig. 8 Scatterplot showing the correlation between utilized fiber separation and THC and S_tO_2, respectively. Correlation coefficients *r* are added for reference.

Table 3 Detailed report on optical and physiological characteristics of human prostate tissue *in vivo*, as measured by our time-resolved instrumentation; prostate volumes (V) are determined from ultrasound images.

				Optical properties (cm^{-1})				Physiological properties	
Patient	Age (yr)	V (cm^3)	Fiber sep. (mm)	$\mu_a(660)$	$\mu_s'(660)$	$\mu_a(786)$	$\mu_s'(786)$	THC (μM)	S_tO_2 (%)
1	57	41	10.1	0.67	11.1	0.56	9.1	300	78
			14.9	0.50	8.9	0.44	6.7	235	80
			17.3	0.48	7.8	0.41	6.6	217	78
2	69	23	10.1	0.59	9.9	0.45	8.6	237	74
			15.1	0.42	10.0	0.34	8.5	177	75
			17.1	0.52	9.7	0.38	7.2	197	72
3	58	26	14.6	0.53	10.3	0.39	8.3	204	72
			21.9	0.55	6.6	0.43	4.7	226	75
			26.6	0.49	6.8	0.39	5.4	206	76
4	70	40	14.6	0.57	8.5	0.50	7.0	266	79
			21.1	0.50	8.2	0.45	6.5	239	80
			26.5	0.50	8.4	0.41	6.4	217	77
5	70	33	14.8	0.56	9.2	0.47	7.4	247	77
			17.7	0.52	10.3	0.40	8.3	212	75
			23.3	0.52	10.7	0.39	8.3	205	73
6	69	36	16.0	0.49	8.0	0.39	6.7	204	76
			21.5	0.24	5.8	0.17	4.6	85	69
			26.4	0.21	5.4	0.17	4.6	85	74
7	67	24	15.5	0.59	7.3	0.59	6.4	318	83
			19.8	0.67	10.6	0.68	10.0	373	84
			23.3	0.50	10.8	0.43	8.9	229	79
8	68	31	16.2	0.53	6.4	0.46	6.0	246	79
			20.4	0.34	7.9	0.28	6.4	143	75
			25.0	0.17	5.3	0.17	4.5	83	80
9	63	26	15.0	0.67	12.4	0.47	10.1	248	71
			19.4	0.55	7.7	0.41	6.5	213	73
			25.0	0.38	10.2	0.35	9.3	187	81
Average	66	31	19	0.49	8.7	0.41	7.1	215	76
Standard deviation	5	7	5	0.13	1.9	0.12	1.6	65	4

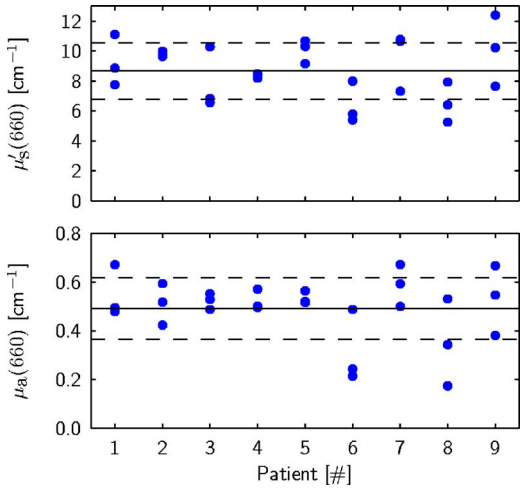

Fig. 9 Inter- and intrapatient variations in 660-nm optical properties. Patients 2 to 5 exhibited homogenous ultrasound images. Solid lines marks the average values, and dashed lines correspond to ± one standard deviation.

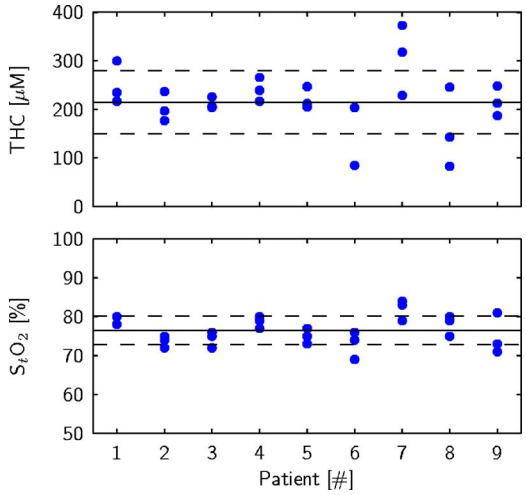

Fig. 11 Inter- and intrapatient variations in hemoglobin parameters. Patients 2 to 5 exhibited homogenous ultrasound images. Solid lines mark the average values, and dashed lines correspond to ± one standard deviation.

lowing observation calls for a separate discussion: derived μ_s' at 916 nm exceeds those at 786 nm in 23 out of 27 measurements. According to the general theory of tissue optics, a reduction of μ_s' is expected. Such behavior was only seen in 4 out of 27 measurements (three out of nine patients). The explanation is very likely to be related to the high absorption and low scattering at 916 nm. In fact, analysis of Monte Carlo simulations indicates a breakdown of diffusion approximation in this regime. Derived μ_s' is closely related to the rising flank of the dispersion curve (early photons), and may be particularly sensitive. Another aggravating circumstance is that such optical properties yield a low degree of broadening (and thus fewer data points), which in turn reduces the performance of the fitting procedure. Refined data evaluation may solve this problem, one option being implementation of Monte-Carlo-based evaluation.

When comparing our results to previously published data, two important facts must be noted. First, differences in patient groups must be taken into account (e.g., untreated or recurrent prostate cancer). The prostate physiology changes drastically upon radiation therapy. An experienced physician can feel such differences during the insertion of brachytherapy needles. Second, previous studies of prostate tissue have employed steady state techniques. Note that the ambiguous appearance of published steady state μ_s' data may indicate a difficulty in separating absorption and scattering using steady-state techniques (cf the published values of μ_s' stated in Table 2). Unfortunately, differences in patient groups prevent these results from being compared to the results of this study. It would thus be very interesting to employ time-resolved spectroscopy also in cases of locally recurrent prostate cancer. On the other hand, in the 600-nm range, μ_{eff} were measured using steady state techniques in patient groups similar to ours. In this respect, the two techniques seem to produce similar data (most derived μ_{eff} values are between 3 and 4 cm^{-1}).

To discuss the correctness of our approach, a few general remarks are given in the following. First, the model used in this study is valid for photon fluence rates. Detected light is collected by cleaved optical fibers, and is thus not a direct measure of fluence rate. Since data evaluation considers only temporal shapes, this fact is, however, not a source of error if the proportionality constant between actual fluence rate and collected light is the same for all photon times of flight. Moreover, the model applies for homogenous media. The prostate

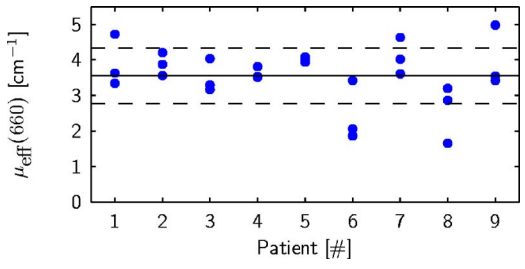

Fig. 10 Inter- and intrapatient variations in 660-nm effective attenuation. Patients 2 to 5 exhibited homogenous ultrasound images. The solid line mark the average value, and dashed lines correspond to ± one standard deviation.

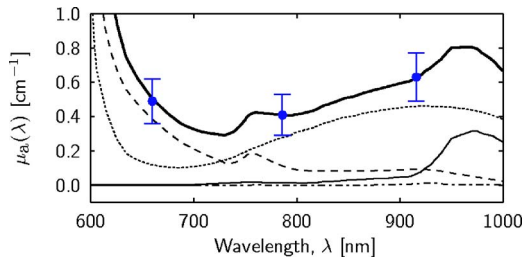

Fig. 12 Synthetic average absorption spectra (bold solid) together with derived absorption coefficients at 660, 786, and 916 nm (mean ± standard deviation). It is constructed using 215 μM THC at 76% oxygen saturation, 70% water and 10% lipids. Contribution spectra are also shown: 51.6-μM Hb (dashed), 163.4-μM HbO_2 (dotted), 70% water (solid), and 10% lipid (dash-dotted).

is, of course, heterogenous, and out of all detected photons, those that have traveled through regions of low attenuation will be overrepresented. One should therefore be careful in interpreting the derived values as true volume averages.

Second, the choice of data range involved in curve fitting occasionally has an influence on the outcome. Finding an optimal fitting range is, however, a complex issue, since the correctness of our model varies with the photon time of flight. For example, early photons are often disregarded since diffusion theory does not describe them very well. In this study, we focus on regions with fairly high photon count rates by choosing to cut the tail of late photons at 20% of maximum (see Sec. 2.2). The reason why later photons are excluded is to avoid a region with many data points at a low signal level, where even small absolute systematic measurement/model errors will have a significant impact on fitted parameters.

Third, as we can see in Eq. (3), the fiber separation is an important parameter in time-resolved spectroscopy. The inferring of fiber separations from ultrasound images is, of course, afflicted with some errors. However, it is unlikely that the error between true and measured separation, r_{true} and r_{meas}, respectively, exceeds 1 mm. From Eq. (3), one finds that errors in fiber separation will produce errors only in derived reduced scattering coefficients. The optimal fit is expected when μ_s' is selected so that

$$\mu_s' r_{\text{meas}}^2 = \mu_s'(r_{\text{true}} + \delta r)^2 = \mu_{s,\text{true}}' r_{\text{true}}^2, \tag{6}$$

where $\mu_{s,\text{true}}'$ is the true reduced scattering coefficient, and δr is the error in fiber separation. The impact of uncertainties regarding fiber separation can be described by the tuning coefficient

$$\gamma_r = \left.\frac{\partial \mu_s'}{\partial \delta r}\right|_{\delta r=0} = \frac{-2\mu_{s,\text{true}}'}{r_{\text{true}}}, \tag{7}$$

which states the change in derived reduced scattering coefficients due to (small) errors in fiber separation. For the case of $\mu_{s,\text{true}}'=8.7\ \text{cm}^{-1}$ and $r_{\text{true}}=20$ mm, one finds that $\gamma_r = 0.87\ \text{cm}^{-1}/\text{mm}$. Hence, a nonnegligible part of the intrasubject variations in derived reduced scattering coefficients may be assigned to errors in fiber separation. However, correlation with ultrasound heterogeneity and the large variations measured in some patients imply that there are significant inherent intrasubject variations.

Finally, the time-resolved approach, in contrast to steady state techniques, should be rather insensitive to bleedings around the needle tips. These bleedings can be thought of as random filters, and may therefore disturb measurements of fluence rate. However, all detected photons must pass the region of bleeding, leaving the temporal shape unchanged.

5 Summary

This study clearly shows that time-resolved spectroscopy is a suitable tool for accessing information on human prostate tissue *in vivo*. By producing consistent estimations of absorption (μ_a), reduced scattering (μ_s'), effective attenuation (μ_{eff}), hemoglobin concentrations, and tissue oxygenation, this technique was able to generate the most complete *in vivo* optical characterization of human prostate tissue published so far. By measuring across three tissue volumes in each prostate, both inter- and intrasubject variations were examined. All derived parameters, with the exception of tissue oxygen saturation, are subject to fairly large intrasubject variation. Interestingly, these variations correlate with the heterogeneity exhibited by acquired ultrasound images.

Acknowledgments

The authors wish to thank the brachytherapy team at the Lund University Hospital, especially Ola Bratt, Inger-Lena Lamm, Per Munck af Rosenschöld, Jonas Nilsson, and Pia Nilsson, for friendly and professional cooperation. We are also grateful to Christoffer Abrahamsson, Ann Johansson, and Johannes Swartling for fruitful discussions, as well as to Johan Stensson for technical assistance during measurements.

References

1. M. S. McPhee, C. W. Thorndyke, G. Thomas, J. Tulip, D. Chapman, and W. H. Lakey, "Interstitial applications of laser irradiation in hematoporphyrin derivative-photosensitized dunning r3327 prostate cancers, *Lasers Surg. Med.* **4**(1), 93–98 (1984).
2. J. L. Camps, S. K. Powers, W. C. Beckman, J. T. Brown, and R. M. Weissman, "Photodynamic therapy of prostate-cancer: an in vitro study," *J. Urol. (Baltimore)* **134**(6), 1222–1226 (1985).
3. T. Windahl, S. O. Andersson, and L. Lofgren, "Photodynamic therapy of localized prostatic cancer," *Langmuir* **336**(8723), 1139–1139 (1990).
4. L. K. Lee, C. Whitehurst, Q. Chen, M. L. Pantelides, F. W. Hetzel, and J. V. Moore, "Interstitial photodynamic therapy in the canine prostate," *Br. J. Urol.* **80**(6), 898–902 (1997).
5. Q. Chen, Z. Huang, D. Luck, J. Beckers, P. H. Brun, B. C. Wilson, A. Scherz, Y. Salomon, and F. W. Hetzel, "Preclinical studies in normal canine prostate of a novel palladium-bacteriopheophorbide (WST09) photosensitizer for photodynamic therapy of prostate cancer," *Photochem. Photobiol.* **76**(4), 438–445 (2002).
6. R. Sroka, D. Zaak, M. Hoppner, R. Muschter, R. Knuchel, A. Perlmutter, and A. Hofstetter, "*In vivo* investigations of photodynamic therapy by means of 5-ALA induced PPIX on canine prostates," *Med. Laser Appl.* **18**(1), 87–90 (1992).
7. D. Zaak, R. Sroka, et al., "Photodynamic therapy of prostate cancer by means of 5-aminolevulinic acid-induced protoporphyrin IX—*in vivo* experiments on the dunning rat tumor model," *Urol. Int.* **72**(3), 196–202 (2004).
8. A. M. Ronn, M. Nouri, L. A. Lofgren, B. M. Steinberg, A. Westerborn, T. Windahl, M. J. Shikowitz, and A. L. Abramson, "Human tissue levels and plasma pharmacokinetics of temoporfin (Foscan(R), mTHPC)," *Lasers Med. Sci.* **11**(4), 267–272 (1996).
9. D. Zaak, R. Sroka, M. Hoppner, W. Khoder, O. Reich, S. Tritschler, R. Muschter, R. Knuchel, and A. Hofstetter, "Photodynamic therapy by means of 5-ALA induced PPIX in human prostate cancer—preliminary results," *Med. Laser Appl.* **18**(1), 91–95 (2003).
10. T. Nathan, D. Whitelaw, et al., "Photodynamic therapy for prostate cancer recurrence after radiotherapy: a phase I study," *J. Urol. (Baltimore)* **168**(4), 1427–1432 (2002).
11. K. Verigos, D. C. H. Stripp, et al., "Updated results of a phase I trial of motexafin lutetium-mediated interstitial photodynamic therapy in patients with locally recurrent prostate cancer," *J. Environ. Pathol. Toxicol. Oncol.* **25**(1–2), 373–387 (2006).
12. K. L. Du, R. Mick, et al., "Preliminary results of interstitial motexafin lutetium-mediated PDT for prostate cancer," *Lasers Surg. Med.* **38**(5), 427–434 (2006).
13. C. M. Moore, T. R. Nathan, W. R. Lees, C. A. Mosse, A. Freeman, M. Emberton, and S. G. Bown, "Photodynamic therapy using meso tetra hydroxy phenyl chlorin (mTHPC) in early prostate cancer," *Lasers Surg. Med.* **38**(5), 356–363 (2006).
14. C. M. Moore, I. M. Hoh, S. G. Bown, and M. Emberton, "Does photodynamic therapy have the necessary attributes to become a future treatment for organ-confined prostate cancer?" *BJU Int.*, **96**(6), 754–758 (2005).

15. J. H. Pinthus, A. Bogaards, R. Weersink, B. C. Wilson, and J. Trachtenberg, "Photodynamic therapy for urological malignancies: past to current approaches," *J. Urol. (Baltimore)* **175**(4), 1201–1207 (2006).
16. W. M. Star, "Light dosimetry *in vivo*," *Phys. Med. Biol.* **42**(5), 763–787 (1997).
17. C. Whitehurst, M. L. Pantelides, J. V. Moore, and N. J. Blacklock, "Optimization of multifiber light delivery for the photodynamic therapy of localized prostate-cancer," *Photochem. Photobiol.* **58**(4), 589–593 (1993).
18. Q. Chen and F. Hetzel, "Laser dosimetry studies in the prostate," *J. Clin. Laser Med. Surg.* **16**(1), 9–12 (1998).
19. L. Lilge, N. Pomerleau-Dalcourt, A. Douplik, S. Selman, R. Keck, M. Szkudlarek, M. Pestka, and J. Jankun, "Transperineal *in vivo* fluence-rate dosimetry in the canine prostate during SnET2-mediated PDT," *Phys. Med. Biol.* **49**(14), 3209–3225 (2004).
20. M. D. Altschuler, T. C. Zhu, J. Li, and S. M. Hahn, "Optimized interstitial PDT prostate treatment planning with the Cimmino feasibility algorithm," *Med. Phys.* **32**(12), 3524–3536 (2005).
21. J. Jankun, R. W. Keck, E. Skrzypczak-Jankun, L. Lilge, and S. H. Selman, "Diverse optical characteristic of the prostate and light delivery system: implications for computer modelling of prostatic photodynamic therapy," *BJU Int.* **95**(9), 1237–1244 (2005).
22. J. Jankun, L. Lilge, A. Douplik, R. W. Keck, M. Pestka, M. Szkudlarek, P. J. Stevens, R. J. Lee, and S. H. Selman, "Optical characteristics of the canine prostate at 665 nm sensitized with tin etiopurpurin dichloride: need for real-time monitoring of photodynamic therapy," *J. Urol. (Baltimore)* **172**(2), 739–743 (2004).
23. A. Johansson, T. Johansson, M. Soto Thompson, N. Bendsoe, K. Svanberg, S. Svanberg, and S. Andersson-Engels, "*In vivo* measurement of parameters of dosimetric importance during photodynamic therapy of thick skin tumors," *J. Biomed. Opt.* **11**(3), 034029 (2006).
24. M. L. Pantelides, C. Whitehurst, J. V. Moore, T. A. King, and N. J. Blacklock, "Photodynamic therapy for localized prostatic cancer—light penetration in the human prostate-gland," *J. Urol. (Baltimore)* **143**(2), 398–401 (1990).
25. M. Essenpreis, "Thermally induced changes in optical properties of biological tissues," Ph.D. Thesis, University College London (1992).
26. C. Whitehurst, M. L. Pantelides, J. V. Moore, P. J. C. Brooman, and N. J. Blacklock, "*In vivo* laser-light distribution in human prostatic-carcinoma," *J. Urol. (Baltimore)* **151**(5), 1411–1415 (1994).
27. Q. Chen, B. C. Wilson, S. D. Shetty, M. S. Patterson, J. C. Cerny, and F. W. Hetzel, "Changes in *in vivo* optical properties and light distributions in normal canine prostate during photodynamic therapy," *Radiat. Res.* **147**(1), 86–91 (1997).
28. L. K. Lee, C. Whitehurst, M. L. Pantelides, and J. V. Moore, "*In situ* comparison of 665 nm and 633 nm wavelength light penetration in the human prostate gland," *Photochem. Photobiol.* **62**(5), 882–886 (1995).
29. L. K. Lee, C. Whitehurst, M. L. Pantelides, and J. V. Moore, "An interstitial light assembly for photodynamic therapy in prostatic carcinoma," *BJU Int.* **84**(7), 821–826 (1999).
30. R. A. Weersink, A. Bogaards, M. Gertner, S. R. H. Davidson, K. Zhang, G. Netchev, J. Trachtenberg, and B. C. Wilson, "Techniques for delivery and monitoring of TOOKAD (WST09)-mediated photodynamic therapy of the prostate: clinical experience and practicalities," *J. Photochem. Photobiol., B* **79**(3), 211–222 (2005).
31. T. C. Zhu, J. C. Finlay, and S. M. Hahn, "Determination of the distribution of light, optical properties, drug concentration, and tissue oxygenation *in vivo* in human prostate during motexafin lutetium-mediated photodynamic therapy," *J. Photochem. Photobiol., B* **79**(3), 231–241 (2005).
32. D. R. Doiron, L. O. Svaasand, and A. E. Profio, "Light dosimetry in tissue: application to photoradiation therapy," *Appl. Spectrosc.* **160**, 63–76 (1983).
33. A. Dimofte, J. C. Finlay, and T. C. Zhu, "A method for determination of the absorption and scattering properties interstitially in turbid media," *Phys. Med. Biol.* **50**(10), 2291–2311 (2005).
34. T. C. Zhu, A. Dimofte, J. C. Finlay, D. Stripp, T. Busch, J. Miles, R. Whittington, S. B. Malkowicz, Z. Tochner, E. Glatstein, and S. M. Hahn, "Optical properties of human prostate at 732 nm measured during motexafin lutetium-mediated photodynamic therapy, *Photochem. Photobiol.* **81**(1), 96–105 (2005).
35. A. H. Barnett, J. P. Culver, A. G. Sorensen, A. Dale, and D. A. Boas, "Robust inference of baseline optical properties of the human head with three-dimensional segmentation from magnetic resonance imaging," *Appl. Opt.* **42**(16), 3095–3108 (2003).
36. C. Abrahamsson, A. Löwgren, B. Strömdahl, T. Svensson, S. Andersson-Engels, J. Johansson, and S. Folestad, "Scatter correction of transmission near-infrared spectra by photon migration data: quantitative analysis of solids," *Appl. Spectrosc.* **59**(11), 1381–1387 (2005).
37. P. Taroni, A. Torricelli, L. Spinelli, A. Pifferi, F. Arpaia, G. Danesini, and R. Cubeddu, "Time-resolved optical mammography between 637 and 985 nm: clinical study on the detection and identification of breast lesions," *Phys. Med. Biol.* **50**(11), 2469–2488 (2005).
38. Y. Hoshi, M. Shimada, C. Sato, and Y. Iguchi, "Reevaluation of near-infrared light propagation in the adult human head: implications for functional near-infrared spectroscopy," *J. Biomed. Opt.* **10**(6), 064032 (2005).
39. T. Svensson, J. Swartling, P. Taroni, A. Torricelli, P. Lindblom, C. Ingvar, and S. Andersson-Engels, "Characterization of normal breast tissue heterogeneity using time-resolved near-infrared spectroscopy," *Phys. Med. Biol.* **50**(11), 2559–2571 (2005).
40. A. Pifferi, A. Torricelli, A. Bassi, P. Taroni, R. Cubeddu, H. Wabnitz, D. Grosenick, M. Moller, R. Macdonald, J. Swartling, T. Svensson, S. Andersson-Engels, R. L. P. van Veen, H. J. C. M. Sterenborg, J. M. Tualle, H. L. Nghiem, S. Avrillier, M. Whelan, and H. Stamm, "Performance assessment of photon migration instruments: the MEDPHOT protocol," *Appl. Opt.* **44**(11), 2104–2114 (2005).
41. M. S. Patterson, B. Chance, and B. C. Wilson, "Time resolved reflectance and transmittance for the noninvasive measurement of tissue optical-properties," *Appl. Opt.* **28**(12), 2331–2336 (1989).
42. T. Nakai, G. Nishimura, K. Yamamoto, and M. Tamura, "Expression of optical diffusion coefficient in high-absorption turbid media," *Phys. Med. Biol.* **42**(12), 2541–2549 (1997).
43. T. Durduran, A. G. Yodh, B. Chance, and D. A. Boas, "Does the photon-diffusion coefficient depend on absorption?" *J. Opt. Soc. Am. A* **14**(12), 3358–3365 (1997).
44. W. Press, S. Teukolsky, W. Vetterling, and B. Flannery, *Numerical Recipes in C: The Art of Scientific Computing*, 2nd ed., Cambridge University Press, Cambridge (1992).
45. G. M. Hale and M. R. Querry, "Optical-constants of water in 200-nm to 200-mum wavelength region," *Appl. Opt.* **12**(3), 555–563 (1973).
46. R. L. P. van Veen, H. J. C. M. Sterenborg, A. Pifferi, A. Torricelli, E. Chikoidze, and R. Cubeddu, "Determination of visible near-IR absorption coefficients of mammalian fat using time- and spatially resolved diffuse reflectance and transmission spectroscopy," *J. Biomed. Opt.* **10**(5), 054004 (2005).
47. S. Prahl, "Optical absorption of hemoglobin," URL http://omlc.ogi.edu/spectra/hemoglobin/index.html(2006).
48. J. C. Schotland, J. C. Haselgrove, and J. S. Leigh, "Photon hitting density," *Appl. Opt.* **32**(4), 448–453 (1993).